available at www.sciencedirect.com

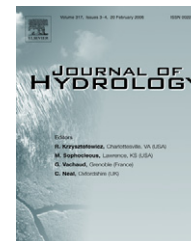**ScienceDirect**

journal homepage: www.elsevier.com/locate/jhydrol

Seepage caused tension failures and erosion undercutting of hillslopes

M.L. Chu-Agor [a], G.A. Fox [b,*], R.M. Cancienne [c], G.V. Wilson [d]

[a] *Department of Biosystems and Agricultural Engineering, Oklahoma State University, 209 Agricultural Hall, Stillwater, OK 74078, United States*
[b] *Department of Biosystems and Agricultural Engineering, Oklahoma State University, 120 Agricultural Hall, Stillwater, OK 74078, United States*
[c] *Formerly, Department of Biosystems and Agricultural Engineering, Oklahoma State University, Currently, Philip Williams and Associates Ltd., Sacramento, CA, United States*
[d] *Hydrologist/Soil Physicist, USDA-ARS National Sedimentation Laboratory, Oxford, MS 38655, United States*

Summary   Seepage has been suggested as an important factor in gully and river bank erosion. This study investigated the underlying mechanisms of instability by seepage in laboratory studies. A 25-cm tall, 50-cm wide, and 20-cm long soil block with a focused inflow reservoir was constructed to investigate seepage gradient forces and the three-dimensional nature of seepage particle mobilization (i.e., seepage erosion) and undercutting. Experiments included sand and loamy sand soil blocks packed at prescribed bulk densities (1.30–1.70 Mg m^{-3}) and with an outflow face at various angles (90°, 75°, and 60°). Constant heads of 15, 25, and 35 cm were imposed on the soil to induce flow. A laser scanner was utilized to obtain the three-dimensional coordinates of the bank and undercut surfaces at approximately 15–30 s intervals. The bulk density of the two different soil types controlled which seepage failure mechanism occurred: (1) tension or ''pop-out'' failures due to the seepage force exceeding the soil shear strength which was being concurrently reduced by increased soil pore-water pressure, or (2) particle entrainment in the seepage flow, particle mobilization, bank undercutting, and bank collapse when the initial seepage force gradient was less than the resistance of the soil block. For cases experiencing particle mobilization and undercutting, seepage erosion initiated as unimodal (i.e., concentrated at one point) or as multimodal (i.e., initiating at several locations across the bank face), and this result was largely controlled by the bank angle. A

---

* Corresponding author. Tel.: +1 405 744 8423; fax: +1 405 744 6059.
  E-mail addresses: maria.agor@okstate.edu (M.L. Chu-Agor), garey.fox@okstate.edu (G.A. Fox), rachel.cancienne@okstate.edu (R.M. Cancienne), glenn.wilson@ars.usda.gov (G.V. Wilson).

five parameter Gaussian function was fitted to the measured three-dimensional undercut shapes to derive parameters for the maximum depth of undercutting, position of the center of the peak, and the vertical and lateral spreads of the undercut. The parameters of this distribution can be useful in the development of improved sediment transport functions and the incorporation of this failure mechanism into hillslope stability models.

Introduction

Seepage has been suggested to potentially play a prominent role in gully and streambank erosion (Abam, 1993; Darby and Thorne, 1996; Crosta and di Prisco, 1999; Rinaldi and Casagli, 1999; Simon et al., 1999). Seepage is now accepted, especially in Europe, as a critically important process in rill and gully development (Faulkner, 2006; Sultan et al, 2004). This research, and its corresponding literature review, are placed in the context of streambank failure but is equally applicable to hillslope failure and gully development in its assessment of seepage mechanisms.

The complex interaction between seepage and other bank stability and instability mechanisms (i.e., fluvial erosion, confining pressure, and vegetation) makes it difficult to fully understand the role of seepage on bank instability. According to Crosta and di Prisco (1999), in order to understand the onset of streambank instability due to seepage, it is important to point out that the collapse is the final result of a complex chain of events taking place during a certain time period. They added that analysis is complex because of the partial saturation of the materials, the three-dimensional geometry of the problem, and the heterogeneity of materials. Hooke (1979) suggested that more detailed work is needed on the effects of soil moisture, the pattern of forces on the bank and the changes in shear strength of the bank material. The ASCE (1998) suggested that methods capable of predicting the stability of streambanks with respect to a range of possible failure mechanisms must be developed.

Some of the complexity regarding seepage stems from the fact that seepage can cause hillslope instability through three different but interrelated mechanisms: (1) increased soil pore-water pressure reducing the shear strength of the soil, (2) seepage gradient forces, and (3) seepage particle mobilization and undercutting. Most research to date has focused specifically on one of these three mechanisms.

Increased soil pore-water pressure

Soil strength or the resisting force which is responsible for bank stability is usually defined using Mohr−Coulomb's equation:

$$s = c' + (\sigma_n - u_w)\tan\phi' \tag{1}$$

where s is the shear strength, c' the effective cohesion, φ' the effective angle of internal friction, σ_n the total normal stress, and u_w the soil pore-water pressure (Whitlow, 1983; Fredlund and Rahardjo, 1993). In unsaturated soils, decreasing matric suction has the effect of increasing the apparent cohesion of the soil, as described by Fredlund and Rahardjo (1993):

$$s = c' + (\sigma_n - u_w)\tan\phi' + (u_a - u_w)\tan\phi^b \tag{2}$$

where u_a the soil pore-air pressure and ϕ^b is the angle indicating the rate of increase in the shear strength relative to matric suction and is generally between $10°$ and $20°$ (Fredlund and Rahardjo, 1993; Simon et al., 1999). Therefore, an increase in pore-water pressure decreases the effective stress of the soil which in turn decreases the shear strength.

Sultan et al. (2004) analyzed the different slope failure events from the COSTA (continental slope stability) target areas (Adriatic margin, Western Mediterranean margin, and Northeast Atlantic margin). Their study identified the relation between triggering mechanisms and causal factors (e.g. slope angle) on one hand and the stress state and geotechnical parameters on the other hand. They concluded that excess pore water pressure was a key parameter for the assessment of slope stability. Rinaldi et al. (2003) monitored and modeled the pore water pressure changes and river bank stability during flow in the Sieve River in Italy. Simulations showed that the development of relatively limited pore water pressure and the disappearance of apparent cohesion were sufficient conditions to trigger a mass failure in a streambank composed predominantly of fine-grained, weakly cohesive soil (silt and sand). Lourenco et al. (2006) investigated the influence of permeability variations on slope behavior by experimental means. Their results revealed no clear link between the failure mode and recorded pore water pressure. Failure was not confined to a single failure mode, but ranged instead from retrogressive slides and lateral spreads.

Seepage gradient forces and tension failures

Seepage forces act on grains of sediment and are proportional to the hydraulic gradient $\frac{\partial\psi}{\partial y}$, where ψ is the matric suction and y is a distance:

$$\tau_s = \rho g d \frac{\partial\psi}{\partial y} \tag{3}$$

where τ_s is the seepage stress, ρ is the density of the fluid, g is gravity, and d is the grain diameter (Lobkovsky et al., 2004). Budhu and Gobin (1996) studied cohesionless slope instability due to ground-water seepage in order to provide bounds on the seepage direction that provoked slope failures, referred to in this research as tension or ''pop-out'' failures. They concluded that slope failures resulting from seepage forces were progressive and the minimum stable seepage direction was reached when seepage was parallel to the cohesionless bank slopes. They also showed that the seepage direction that initiates static liquefaction depends on the slope angle and the soil unit weight.

Seepage particle mobilization and undercutting (seepage erosion)

Despite the research conducted on bank instability by increased soil pore-water pressure and tension or ''popout'' failure by seepage forces, our ability to predict bank failure due to seepage particle mobilization (i.e., entrainment in the seepage flow or seepage erosion) remains limited. Although seepage erosion has been observed to occur before massive bank slumping (Bradford and Piest, 1977), it is not until recently that it has been highlighted as a potential failure mechanism of streambanks particularly on the recession limb of the streamflow hydrographs (Fox et al., 2007a; Wilson et al., 2007).

On banks with enough resistance to overcome seepage forces, the seepage gradient can cause particle mobilization when the velocity of water exiting the bank exceeds the critical shear stress leading to bank undercutting. Several studies have incorporated the seepage force given by Eq. (3) into equations for particle mobilization, such as Lobkovsky et al. (2004) who modified the Shields number to include this seepage force and Fox et al. (2006) who derived a seepage erosion sediment transport function with an excess critical discharge formulation. Seepage particle mobilization and undercutting was studied by Fox et al. (2006, 2007a,b) and Wilson et al. (2007) in their two-dimensional lysimeter experiments and bank stability modeling. Wilson et al. (2007) and Chu-Agor et al. (in press) performed step-wise dynamic analysis of the effect of changes in the hillslope geometry due to undercutting on stability. Their work demonstrated that bank stability decreased exponentially as undercutting increased. However, a fully integrated variably saturated flow model with a dynamic geometric and geotechnical model to predict hillslope failure is still lacking. Knowledge on the three-dimensional structure of seepage entrainment and undercutting is needed for this dynamic hydraulic and geotechnical modeling.

Objectives of current study

In this study, the hydraulic conditions producing seepage failure mechanisms (i.e., reduced soil shear strength, seepage gradient forces, and seepage particle mobilization and undercutting) were evaluated. We established the limiting conditions for tension or ''pop-out'' failures by seepage gradient forces as well as investigated the three-dimensional nature of seepage particle mobilization and undercutting. Therefore, this study was one of the first studies to consider multiple seepage mechanisms simultaneously.

Method and materials

Experimental setup and data collection

A three-dimensional soil block was constructed in a Plexiglas box (Fig. 1). The box had two compartments: (1) a focused water reservoir (10 cm high by 10 cm wide centered at the bottom of the back face of the soil block) where a constant water head was maintained, and (2) the soil compartment which simulated a single layered hillslope, gully sidewall, or streambank with varying bank angles, α'. Two
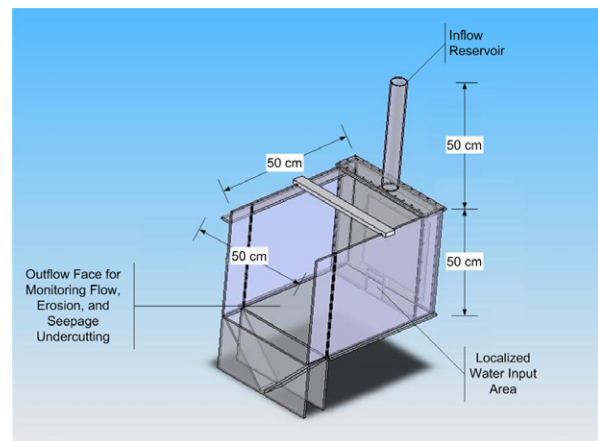

Figure 1 Three-dimensional soil block used to simulate seepage instability of single-layer, repacked soil banks. The inflow reservoir is capable of producing seepage heads up to 100 cm.

different soil textures were used for these experiments: sand and loamy sand. Each soil type was packed in the box at various bulk densities (ρ_b): 1.30, 1.45, and 1.60 Mg m^{-3} for the sand and 1.30, 1.45, 1.50, 1.60, and 1.70 Mg m^{-3} for the loamy sand. Dimensions of the soil block in all experiments were 25 cm high, 50 cm wide and 20 cm long. Also, all experiments were run in duplicate. This research did not evaluate differences in regard to bank height, because Chu-Agor et al. (in press) demonstrated that bank height only impacts initial stability of the bank, not the seepage mechanisms. The bottom of the soil block was lined with a 2.5 cm densely packed clay layer to serve as a restrictive layer. The rest of the block was packed with soil to the desired ρ_b in 2.5 cm lifts. All soil was packed when the soil had reached near residual soil moisture content (i.e., 0.05–0.10 g water per g soil). The soil was then cut to simulate various bank angles, α' (90°, 75°, and 60°) such that the horizontal centerline for each bank remained 20 cm away from the water inlet. For the experiments, hydraulic heads (H) of 15, 25, or 35 cm were maintained in the inflow reservoir using a Marriott-type infiltrometer.

Data collected during the experiments included the flow arrival time at the bank face, the time of seepage erosion initiation, seepage erosion as a function of time, and the volume of bank collapse. During the experiment, seepage erosion particle mobilization and undercutting was monitored over time using a three-dimensional laser scanner (3D Digital Corporation, Sandy Hook, CT). This laser scanner was a medium range scanning instrument with resolutions of 135 µm at a scanning distance of 300 mm or 210 µm at a scanning distance of 650 mm. The point density of the scan was 255 by 1000. For the laboratory experiments, all scans were captured within 650 mm of the bank face. Data from the 3D scanner were used to characterize the hydraulic controls producing a given seepage mechanism. Scanned images were exported to an ASCII file in terms of the XYZ coordinates of the point cloud. The XYZ coordinates were then used to create 2.0 mm square grids using the inverse to distance power algorithm. A program was developed to compute the eroded volume by subtracting the scanned surface at a given time from the scanned surface of the
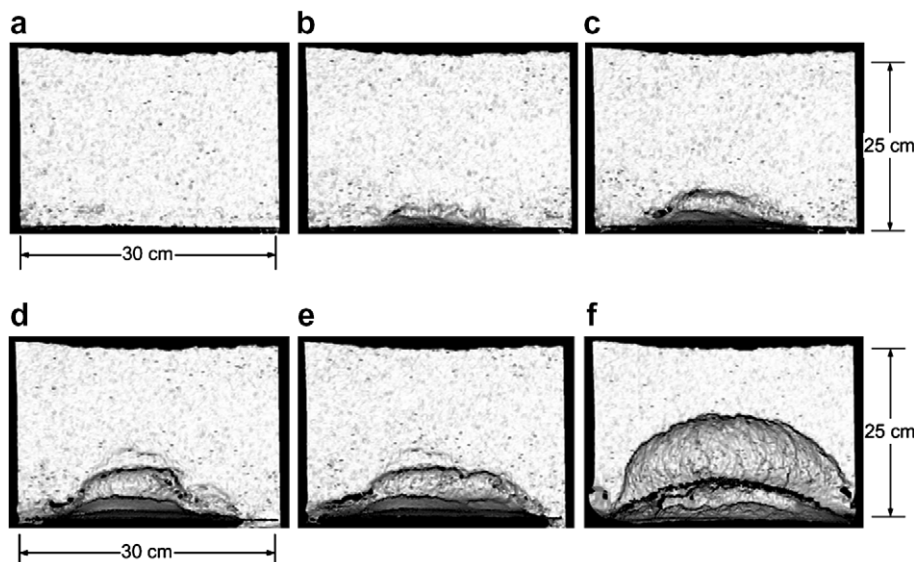
Figure 2 Example of the eroded surface by seepage particle mobilization captured using the three-dimensional laser scanner. Each scan represents a different time during the experiment: (a) original bank face, (b) and (c) illustrate the start of the seepage particle mobilization and undercutting, (d) and (e) illustrate continued undercut growth, and (f) illustrates the bank after small-scale sapping failure on the bank slope.

initial time. An example of the eroded surface by seepage particle mobilization is shown in Fig. 2.

Analysis of stability with seepage gradient forces

Tension or ''pop-out'' failures, where the driving static forces exceed the resisting static forces resulting in a block failure with tension crack formation, have been analyzed by various researchers (i.e., Budhu and Gobin, 1996), primarily by assuming the sediment was non-cohesive. The factor of safety (FS) for a cohesionless slope under a steady-state regime was derived by Budhu and Gobin (1996) as

$$FS = \frac{\left[\left(\frac{\gamma'}{\gamma_w}\right)\cos\alpha' - \sin\alpha'\cot\lambda\right]\tan\phi'}{\left(\frac{\gamma'}{\gamma_w} + 1\right)\sin\alpha'} \quad (4)$$

where γ' is the submerged unit weight of the soil, γ_w the unit weight of water, α' the bank angle, ϕ' the friction angle, and λ the direction of the seepage vector measured clockwise from the inward normal to the bank slope. The failure plane considered in this equation is parallel to the bank slope. This equation was used to investigate the tension or ''pop-out'' failure by seepage gradient forces observed in the three-dimensional soil block experiments. Since the direction of the seepage vector was needed in the equation, an uncalibrated two-dimensional seepage model (SEEP/W) was used to predict the direction of the vector within the flow domain using laboratory measured soil hydraulic parameters as functions of the soil ρ_b. The two-dimensional model was assigned a constant head boundary at the inlet and utilized the soil parameters for each experimental setup discussed later.

In general, the simulation showed two possible directions of the steady-state seepage vector: $90 \leqslant \lambda \leqslant 180$ at the inlet and $180 \leqslant \lambda \leqslant 270$ at the drainage face (Fig. 3). The FS was computed using these ranges of λ for the loamy sand

and sand with ρ_b equal to 1.50 Mg m^{-3} and 1.30 Mg m^{-3}, respectively. Eq. (4) consistently predicted failure (i.e., FS < 1.0) for $90 \leqslant \lambda \leqslant 180$ (at inlet); however, for $180 \leqslant \lambda \leqslant 270$ at the drainage face, it yielded negative FS values which indicated that for cohesionless soil with $30 \leqslant \alpha' \leqslant 90$ and $180 \leqslant \lambda \leqslant 270$, this equation did not apply; i.e., the failure plane was not parallel to the slope as assumed for these conditions.

For cohesionless dry soil, the maximum stable slope with no external load is its angle of internal friction (Budhu and Gobin, 1996). In the laboratory experiments, the soil block was able to hold the 90° slope because of its increased cohesion due to packing, thereby acting as a cohesive soil mass. In order to consider the effects of cohesion, a new FS equation was derived for failure planes perpendicular and parallel to the bank slope to take into account the two possible directions of the seepage vector.

The FS is generally defined as the ratio of the resisting forces to the driving forces. The driving forces were the vector components of the seepage force and weight perpendicular to the failure plane, while the resisting forces were equal to the shear strength of the soil defined by Mohr–Coulomb equation. Consider a soil element (Fig. 4) with unit width. At failure plane y–y, the FS can be written as the ratio of the shear strength of the soil ($c'A_s + \sigma'\tan\phi'$) divided by the sum of the weight and seepage forces parallel to the failure plane (y–y), i.e., $W\sin\alpha' + f_s\sin\lambda$:

$$FS = \frac{c'A_s + \sigma'\tan\phi'}{W\sin\alpha' + f_s\sin\lambda} \quad (5)$$

where c' is the cohesion, A_s is the sheared area, σ' is the effective normal force which is the resultant of the forces acting perpendicular to the failure plane (y–y), W is the weight of the soil element and f_s is the seepage force on the element. For plane y–y, the effective normal force is
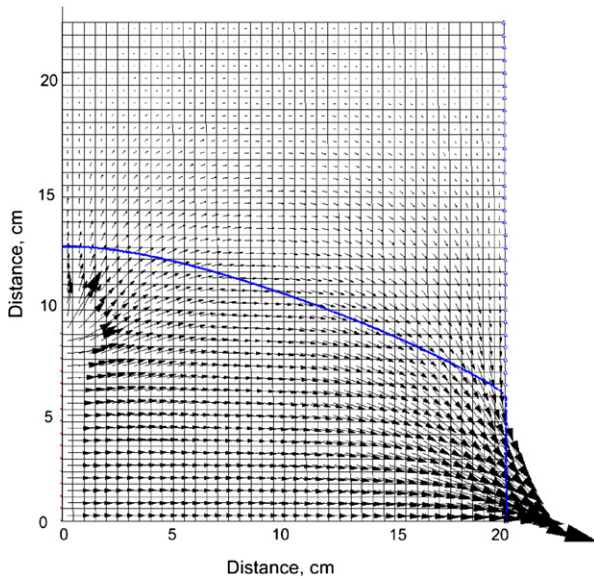
$$\sigma' = W\cos\alpha' - f_s\cos\lambda \quad (6)$$

Figure 3 Seepage vectors as simulated by SEEP/W for a 90° sand bank with an inflow reservoir head of 15 cm and a bulk density, ρ_b, of 1.30 Mg m^{-3}.
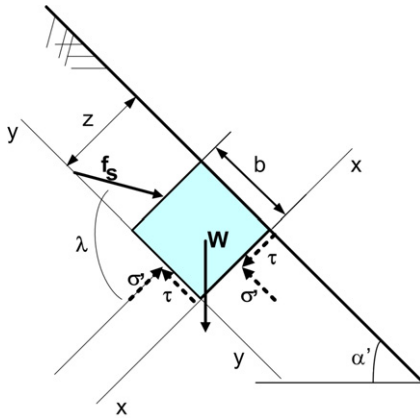

Figure 4 Free-body diagram of a soil element subjected to seepage gradient forces considering two possible failure planes, yy and xx. W is the weight of the soil element; σ' is the effective normal force; τ is the shear stress; f_s is the seepage force on the element; α' the bank angle; λ is the direction of the seepage vector measured clockwise from the inward normal to the bank slope; z is the width of the failure block; and b is the height of the failure block.

where W and f_s are given by

$$W = \gamma'V \tag{7}$$

$$f_s = i\gamma_w V \tag{8}$$

where i is the magnitude of the hydraulic gradient (i.e., $\sin\alpha'/\sin\lambda$) and V is the volume of the soil element. Substituting Eq. (6)–(8) into Eq. (5) results in the following:

$$FS = \frac{c'A_s + (\gamma'V\cos\alpha' - i\gamma_w V\cos\lambda)\tan\phi'}{\gamma'V\sin\alpha' + i\gamma_w V\sin\lambda} \tag{9}$$

Dividing through by V and γ_w, the FS equation along failure plane y–y is given by

$$FS = \frac{\frac{c'}{z\gamma_w} + \left(\frac{\gamma'}{\gamma_w}\cos\alpha' - \sin\alpha'\cot\lambda\right)\tan\phi'}{\left(\frac{\gamma'}{\gamma_w} + 1\right)\sin\alpha'} \tag{10}$$

where A_s in a two-dimensional model is represented by the linear distance z, which corresponds to the distance from the bank face to the failure plane. Similarly, the factor of safety along failure plane x–x can be written as

$$FS = \frac{c'A_s + \sigma'\tan\phi'}{f_s\cos\lambda - W\cos\alpha'} \tag{11}$$

where $\sigma' = W\sin\alpha' + f_s\sin\lambda$. The FS can then be written as

$$FS = \frac{\frac{c'}{b\gamma_w} + \left(\frac{\gamma'}{\gamma_w} + 1\right)\sin\alpha'\tan\phi'}{\sin\alpha'\cot\lambda - \frac{\gamma'}{\gamma_w}\cos\alpha'} \tag{12}$$

where A_s in a two-dimensional model is represented by the linear distance b, which corresponds to the height of the bank.

Eqs. (10) and (12) were used to compute the FS at two sections in the flow domain: close to the inlet where $90 \leqslant \lambda \leqslant 180$ and near the drainage face where $180 \leqslant \lambda \leqslant 270$. For Eq. (10), z was assumed to be 0.20 m because tension cracks were observed to form at that section of the soil block when tension or "pop-out" failure occurred. For Eq. (12), b was assumed equal to 0.20 m, which was where the maximum seepage vector emerged from the bank. The FS was also computed for the same hydraulic conditions (i.e. same H and α') but different ρ_b in order to explain the occurrence of tension or "pop-out" failure.

Trends in seepage erosion and undercutting

For cases with seepage particle mobilization and undercutting, the shape of the eroded surface was investigated for each of the seepage headcuts. A five parameter Gaussian function was fitted to the data:

$$z(x,y) = A\exp\left[-\left\{\left(\frac{x-x_0}{\sigma_x}\right)^2 + \left(\frac{y-y_0}{\sigma_y}\right)^2\right\}\right] \tag{13}$$

where $z(x,y)$ is the measured seepage headcut from the original bank face, A is the amplitude or maximum distance of seepage erosion, x_0 and y_0 is the center of the amplitude, and σ_x and σ_y are spreads of the seepage headcut. The variables σ_x and σ_y are related to the full width at half-maximum (FWHM$_j$) of the Gaussian function:

$$\text{FWHM}_j = 2\sqrt{2\ln(2)}\sigma_j \tag{14}$$

where j is either x or y (Weisstein, 1999). This function was selected because the five parameters could be estimated from measurable characteristics of the headcut.

Each image generated from the scanner was used to identify the initial mode of erosion: unimodal or multimodal. Unimodal erosion represents undercutting that is focused at a single point on the bank face whereas multimodal represents erosion that initiated at more than one location. With this data, trends were investigated between the depth and width of undercutting as functions of soil type, ρ_b, α', and H.

Soil property analysis

For the two soils investigated in this research, samples extracted from the soil block setup (sampled in triplicate) were analyzed in the laboratory to determine particle size distribution and soil hydraulic properties (saturated hydraulic conductivity, K_s, and the soil water retention curve parameters) relative to ρ_b. Particle size analysis was determined by sieve analysis for particles larger than 0.075 mm and the hydrometer method for particles less than 0.075 mm (ASTM Standards D422-63).

The saturated hydraulic conductivity, K_s, was determined on extracted soil cores with bulk densities of 1.30, 1.45, and 1.60 Mg m^{-3} for the sand and 1.50, 1.60, and 1.70 Mg m^{-3} for the loamy sand using a falling head permeameter. The K_s was computed by fitting the measured head loss at time t to the following equation (McWhorter and Sunada, 1977):

$$K_s = \frac{a_p L}{A_{sc} t} \ln \frac{\Delta h_0}{\Delta h(t)} \tag{15}$$

where L is the length of the sample, A_{sc} is the horizontal area of the soil column, a_p the horizontal area of the piezometer, Δh_0 is the initial head (at $t = 0$), and $\Delta h(t)$ is the head at time t.

Water retention was determined on the extracted soil cores using standard test methods (ASTM Standards D3152 and D2325). Water retention data were modeled with RETention Curve (RETC) with the van Genuchten equation using the Mualem assumption (van Genuchten et al., 1991):

$$\theta(h) = \begin{cases} \theta_r + \frac{\theta_s - \theta_r}{[1+|ah|^n]^m} & h < 0 \\ \theta_s & h \geqslant 0 \end{cases} \tag{16}$$

$$K(h) = K_s S_e \left[1 - (1 - S_e^{1/m})^m \right]^2 \tag{17}$$

where S_e is the effective saturation; a (L^{-1}) and n are empirical parameters; $m = 1 - 1/n$; θ_s is the saturated water content; θ_r is the residual water content; and h the pressure head. These soil hydraulic parameters were used in the SEEP/W modeling for deriving the seepage vector direction.

Samples were also analyzed to determine geotechnical properties: effective cohesion (c') and internal angle of friction (φ'). The strength properties of the soil used in the experiments were determined using a direct shear test (ASTM Standards D3080-98). The shear strength was measured under unsaturated moisture conditions mimicking the condition of the packed soil block. Samples were prepared by compacting the soil to a given ρ_b. Three test specimens for each soil type and ρ_b were tested under different normal loads (4.0, 6.0, and 10.0 kg). For a given normal force, the maximum shear stress was determined from the peak of shear stress versus horizontal deformation curve. The soil strength parameters (c' and φ') were derived from Mohr's failure envelope.

Results and discussion

Soil physical, hydraulic, and geotechnical characterization

Hydraulic and geotechnical characteristics are documented in Tables 1–3 for both the sand and loamy sand soils at the

Table 1 Particle size distribution and mean particle size (d_{50}, mm) for the two soils used in the soil block experiments

Soil texture	% Sand	% Silt	% Clay	d_{50}, mm
Sand	99.3	0.7	0.0	0.33
Loamy sand	84.5	13.4	2.1	0.24

various ρ_b investigated in this research. The entry pressure head, a, for the loamy sand was less than a for the sand (Table 2) and the loamy sand soil possessed a one order of magnitude lower K_s than the sand (Table 3). The van-Genuchten curve fit parameters a, n, and θ_r appeared independent of ρ_b, while θ_s and K_s increased with decreased ρ_b (Tables 2 and 3). For example, the K_s for the sand soil at $\rho_b = 1.60$ Mg m^{-3} was almost four times less than K_s at $\rho_b = 1.30$ Mg m^{-3} (Table 3). The c' and φ' were both functions of the soil ρ_b: both c' and φ' linearly increased with increased ρ_b (Table 4). In fact, the ''best-fit'' linear trend lines between c' and ρ_b for the sand and loamy sand soils had an $R^2 = 0.80$ and 0.85, respectively.

Seepage mechanisms: erosion and undercutting versus tension/''pop-out'' failures

The ρ_b for the two different soil types (i.e., sand and loamy sand) controlled the primary seepage mechanism of the failure process. Seepage resulted in an eventual bank collapse either through: (1) tension or ''pop-out'' failures when the force of the seepage was greater than the resistance of the soil that further decreased as a result of reduced shear strength from increased soil pore-water pressure, and (2) particle mobilization (i.e., seepage erosion) and bank undercutting when the seepage force gradient was less than the initial resisting force of the soil block with eventual bank collapse due to the combined forces from seepage and the buildup of pore-water pressure (Table 5).

For these experimental conditions, changes in the ρ_b did not significantly influence the $\frac{\partial \psi}{\partial y}$ in the soil profile and correspondingly the seepage force, as will be discussed below. However, decreasing the ρ_b decreased the resistance of the soil by reducing the total normal stress, c' and φ' as shown in Table 4. This reduction in the resistance of the soil varied based on soil type and along with variability in the driving forces controlled the critical point at which the force of failure became greater than the force of resistance. When the resistive forces are equal to the driving forces without undercutting, pop-out failure occurs. The x-intercept in Fig. 5 corresponded to the ρ_b (therefore the combination of c' and φ') at which the resistive forces became equal to the driving forces without undercutting. Tension or ''pop-out'' failures due to seepage gradient forces were observed for all experimental conditions (i.e., H of 15, 25, and 35 cm and α' of 90, 75, and 60°) when the ratio of the bulk density to the soil grain density, ρ_b/ρ_s (where ρ_b was assumed to be 2.65 Mg m^{-3} to provide a convenient way to non-dimensionalize the ρ_b), of the sand was less than 0.49. For the loamy sand, the critical ρ_b/ρ_s between the two failure mechanisms was approximately 0.58 (Fig. 5). Results were consistent among duplicate experiments for each set of experimental

Table 2 Soil water retention curves estimated using RETC based on pressure plate experiments for the sand and loamy sand soils at the bulk densities used in the soil block experiments

Soil type	Bulk density (Mg m^{-3})	θ_r (cm^3 cm^{-3})	θ_s (cm^3 cm^{-3})	a (cm^{-1})	n	R^2
Sand	1.60	0.05 (0.01)	0.40 (0.00)	0.031 (0.010)	1.33 (0.04)	0.94
Sand	1.45	0.05 (0.01)	0.46 (0.00)	0.026 (0.002)	1.28 (0.02)	0.96
Sand	1.30	0.06 (0.03)	0.51 (0.00)	0.048 (0.018)	1.22 (0.03)	0.92
Loamy Sand	1.70	0.06 (0.03)	0.36 (0.00)	0.019 (0.003)	1.33 (0.16)	0.96
Loamy Sand	1.60	0.04 (0.00)	0.40 (0.00)	0.026 (0.012)	1.23 (0.06)	0.94
Loamy Sand	1.50	0.04 (0.00)	0.43 (0.01)	0.017 (0.011)	1.27 (0.05)	0.90

Reported values are averages of three replicates (standard deviations given in parentheses).

Table 3 Saturated hydraulic conductivity (K_s) measured using constant head permeameter test for varying bulk densities of the sand and loamy sand soils

Soil type	Bulk density, ρ_b (Mg m^{-3})	Saturated hydraulic conductivity, K_s (cm s^{-1})
Sand	1.60	0.0077
	1.45	0.0176
	1.30	0.0284
Loamy sand	1.70	0.0006
	1.60	0.0012
	1.50	0.0034

Table 4 Geotechnical and erodibility properties (effective cohesion, internal angle of friction and critical shear stress) of the sand and loamy sand soils

Soil type	Bulk density, ρ_b (Mg m^{-3})	Effective cohesion, c' (kPa)	Internal angle of friction, φ' (degrees)
Sand	1.60	3.4	40.6
	1.45	2.0	38.4
	1.30	0.5	26.5
Loamy Sand	1.70	7.4	41.9
	1.60	4.9	39.1
	1.50	2.5	36.2

conditions. We hypothesize that greater partially saturated weight (i.e., total weight) was present along the failure plane in the loamy sand soil because of the greater residual moisture content at packing, lower K_s, and lower a (i.e., higher entry pressure head). This greater partially saturated or total weight in the loamy sand soil led to higher driving forces and less resistive strength as the partial saturation reduced the apparent cohesion. Because the driving force and reduced apparent cohesion were lower for the sand as compared to the loamy sand, the threshold for observed seepage undercutting was reached earlier in the sand (Fig. 5).

For higher ρ_b and therefore higher resistive strength beyond this critical ρ_b/ρ_s, the amount of resistive force exceeded the driving force and a stable bank developed. This stable bank did not fail unless undercutting also occurred. Therefore, for these experiments, particle mobilization and undercutting generally occurred under cases of higher ρ_b because of the increased initial bank resistance to the seepage force. Chu-Agor et al. (in press) demonstrated that seepage undercutting exponentially reduced the bank stability with increased amplitude, A, which in this research eventually led to cantilever failures due to seepage particle mobilization and the induced moment by undercutting. It is expected that for exceedingly higher H (i.e., greater than 35 cm), pop-out failure would be observed at greater ρ_b because of the overriding affect of seepage gradient forces.

It is hypothesized that the critical ρ_b/ρ_s will increase for soil types with greater clay content and therefore greater c', dependent on changes in the ρ_b relative to soil type. Considering this hypothesis, the occurrence of these immediate collapses, referred to as tension or ''pop-out'' failures, precludes bank failure by seepage erosion and undercutting being observed in the field. For the non-cohesive seepage layers observed in the field by Wilson et al. (2007), the ρ_b for the loamy sand was reported to be 1.50 Mg m^{-3} (i.e., ρ_b/ρ_s = 0.57), which occurred near the boundary of tension or ''pop-out'' failures observed in this research. They observed seepage undercutting by mobilization of soil particles but did not observe the bank failures in progress in situ. They did observe post-failure evidence of undercutting by seepage erosion in situ. It is possible that these stream banks also experienced tension or ''pop-out'' failures given the hydraulic gradients imposed on the sediment. The stream restoration project reported by Lindow (2007) was undermined due to bank collapses hypothesized to be due to seepage. Due to the cohesions of the banks (i.e., 10.7 to 17.7 kPa), particle mobilization by seepage flow was probably limited. Instead, Lindow (2007) observed in two-dimensional lysimeter experiments with a repacked bank (10-cm of sand at ρ_b = 1.30 Mg m^{-3} underlying 15-cm of sandy clay loam) that the tension or ''pop-out'' failures of this underlying layer eventually led to undermining of the entire bank.

Table 5 Observed seepage erosion volume (V_{SE}), volume (V_{BF}) of soil loss by bank failure, and amplitude or maximum distance of undercutting (A) prior to bank collapse, relative to experimental soil block conditions (α' = bank angle, H = inflow water reservoir head, and ρ_b = soil bulk density)

α' (degrees)	H (cm)	Sand				Loamy sand			
		ρ_b (Mg m⁻³)	A (cm)	V_{SE} (cm³)	V_{BF} (cm³)	ρ_b (Mg m⁻³)	A (cm)	V_{SE} (cm³)	V_{BF} (cm³)
90	15	1.60	4.9	592	6672	1.70	6.1	1448	6145
		1.45	4.9	475	6465	1.60	2.3	130	5235
		1.30	PO*	PO	5727	1.50	PO	PO	4811
						1.45	PO	PO	6134
						1.30	PO	PO	4711
90	25	1.60	6.3	781	6354	1.70	3.0	221	3285
		1.45	4.2	252	6560	1.60	3.4	282	2975
90	35	1.60	4.3	183	6609	1.70	1.5	26	3807
		1.45	3.0	141	NA[a]	1.60	3.1	180	5574
75	15	1.60	6.2	867	4870	1.70	5.2	937	4666
		1.45	2.5	94	4185	1.60	3.4	305	4239
		1.30	PO	PO	NA				
75	25	1.60	6.2	800	5996	1.70	3.5	345	2856
		1.45	2.9	177	3325	1.60	3.6	333	3693
75	35	1.60	5.8	577	5791	1.70	2.8	216	3429
		1.45	2.8	143	2924	1.60	2.6	213	4409
60	15	1.60	6.5	1137	5842	1.70	6.7	1492	5348
		1.45	4.4	437	4713	1.60	6.2	846	4966
60	25	1.60	6.6	814	5082	1.70	3.8	306	3366
		1.45	6.0	744	5034	1.60	5.3	288	4117
60	35	1.60	5.6	508	4422	1.70	5.8	1191	4196
		1.45	7.0	198	5170	1.60	4.4	626	3650

Values are averages of at least duplicate experiments. *PO: tension or ''pop-out'' failure due to pore-water pressure gradient without seepage undercutting.

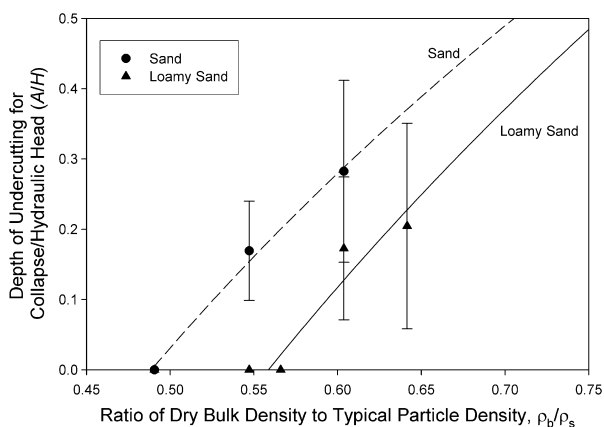[a] Data not collected during the experiment.

Figure 5 Relationship between maximum depth of undercutting (i.e., amplitude, A) required for a bank failure and the bulk density (ρ_b) non-dimensionalized by the particle density (ρ_s) of the soil. The symbols represent the averages relative to varying bank slope and water head for each soil type.

For cases where seepage undercutting occurred, the depth of undercutting required for a bank collapse was most dependent on the soil ρ_b as compared to α' or H for these experimental conditions (Fig. 5). The error bars shown in Fig. 5 represent variability due to the imposed inflow H and α'. For experiments with the same soil type, α' and H, the required amplitude of undercutting (A), which generally fell within the range of 2.0–7.0 cm, decreased as the ρ_b decreased (Table 5) due to the corresponding decrease in the bank's resistive force (i.e., c') (Table 4). Correspondingly, the cumulative volume of seepage erosion required to cause bank failure decreased as the ρ_b decreased (Table 5). The loamy sand soil generally required equivalent to slightly lower amplitudes of undercutting for bank collapse than the sand experiment based on experiments with the same ρ_b (i.e, 1.60 Mg m⁻³), α' (90°, 75°, and 60°), and H (15, 25 and 35 cm). This effect was most likely due to the approximately equivalent c' for the two soils when packed to the same ρ_b (i.e, 1.60 Mg m⁻³). Therefore, sediment transport models for seepage erosion should include an explicit consideration for the ρ_b of the non-cohesive sediment. The sediment transport functions of Howard and McLane (1988) and Fox et al. (2006) include an empirical packing coefficient, along with the K_s, that implicitly account for ρ_b.

As expected due to the lower ρ_b, the time for bank failure in experiments with tension or ''pop-out'' failures was shorter than the time of failure for experiments with seepage particle mobilization. For experiments on the same soil with equivalent α' and ρ_b, an increase in H generally resulted in less seepage erosion and correspondingly lower amplitudes required for bank failure (Table 5). The increased H theoretically resulted in greater soil pore-water

pressures in the overlying topsoil which reduced the shear strength of the soil. These results mimic those of Fox et al. (2006, 2007a,b) and Wilson et al. (2007) in that seepage particle mobilization and increased soil pore-water pressure were both important processes leading to bank failures. As α' decreased for a particular ρ_b and H, the amplitude of the seepage undercut required for bank collapse increased. This result was fundamentally obvious since lower α' resulted in initially more stable banks (higher factor of safety), requiring a greater amplitude of seepage undercut to cause a failure (Chu-Agor et al., in press).

No significant differences (significance level of 0.05) were observed between the mass and volumes of collapsed banks for tension or ''pop-out'' failures as compared to seepage undercutting (Table 5). For the sand soil, the average volume of bank collapse by tension or ''pop-out'' failure (i.e., three experiments with ρ_b equal to 1.30 Mg m^{-3}) was 5727 cm^3 compared to 5373 cm^3 for the seepage undercut banks (P-value = 0.72). The mass of collapsed sand banks by tension or ''pop-out'' failures was 7.5 kg compared to 8.3 kg for seepage undercut banks (P-value = 0.60). For the loamy sand, the average volume of tension or ''pop-out'' failures (i.e., four experiments with ρ_b less than 1.50 Mg m^{-3}) was 5092 cm^3 compared to 4220 cm^3 for seepage particle mobilization and undercutting (P-value = 0.11). The average mass of tension or ''pop-out'' failures was 7.1 kg compared to 7.0 kg for seepage particle mobilization and undercutting (P-value = 0.88).

The phase diagram of Lobkovsky et al. (2004) developed for small α' (i.e., $\alpha' < 12°$) suggests that α' greater than 12° will always experience slumping. This was also verified by our laboratory experiments. The uniqueness of this research was that the mechanism of the slumping (i.e., particle mobilization and undercutting versus tension or ''pop-out'' failure) was highlighted relative to the soil character-istics. Existing slope stability equations for Coulomb failure of non-cohesive slopes should be able to predict failures by seepage forces if banks truly behave as non-cohesive and bank angles are less than the angle of internal friction. However, bank stability analyses capable of modeling seepage particle mobilization and undercutting due to seepage erosion are limited. Some work has been done on the effect of the change in the geometry of the bank due to undercutting on bank failure such as the static analyses reported by Wilson et al. (2007) and the step-wise dynamic analysis by Chu-Agor et al. (in press). However, fully integrated variably saturated flow model with a dynamic geometric and geotechnical model to predict bank failure is still lacking.

Analysis of stability with seepage gradient forces

The theoretical FS for non-cohesive and cohesive banks verified the experimental observations in Fig. 5. Tension or ''pop-out'' failures occurred when a critical failure plane with FS < 1.0 developed within the flow domain. In the soil block experiments, the critical failure plane was located close to the inlet where the seepage force was directed upward. Upward seepage force reduced the effective normal force on the soil, resulting in lower soil shear strength. The magnitude of the seepage force and the reduced cohesion due to lower ρ_b were the reasons for the tension or ''pop-out'' failure observed in the soil block experiments.

Table 6 shows the computed FS with and without cohesion at two different locations in the flow domain. When cohesion was not considered, the banks were unstable for most values of λ. However, the soil used in the experiment was cohesive because of packing effects. The measured c' and ϕ' were found to be dependent on the ρ_b. Therefore, a cohesionless assumption did not represent the condition of the soil used in this experiment.

Table 6 Factor of safety (FS) for the sand (S) and loamy sand (LS) banks computed at two different locations in the flow domain. Close to the inlet, the seepage vector is directed at $90 \leqslant \lambda \leqslant 180$ and the valid failure plane is $y-y$ (see Fig. 4)

Bank	ρ_b (Mg m^{-3})	α' (degrees)	c' (kPa)	φ' (degrees)	Observed seepage mechanics (m)	FS at inlet − Eq. (10) (Maximum λ, degrees)	FS at outlet − Eq. (12) (Maximum λ, degrees)
S	1.30	90	0.0	26.5	PO[a]	0.23 (130)	0.52 (210)
	1.30	75	0.0	26.5	PO	0.38 (140)	0.61 (210)
	1.45	90	0.0	38.4	SU[b]	0.35 (130)	0.87 (210)
	1.60	90	0.0	40.6	SU	0.36 (130)	0.99 (210)
S	1.30	90	0.5	26.5	PO	0.38 (130)	0.68 (210)
	1.30	75	0.5	26.5	PO	0.52 (140)	0.78 (210)
	1.45	90	2.0	38.4	SU	0.89 (130)	1.47 (210)
	1.60	90	3.4	40.6	SU	1.22 (130)	1.98 (210)
LS	1.50	90	0.0	36.2	PO	0.32 (130)	0.83 (210)
	1.60	90	0.0	39.1	SU	0.34 (140)	0.94 (210)
	1.70	90	0.0	41.9	SU	0.37 (130)	1.06 (210)
LS	1.50	90	2.5	36.2	PO	0.98 (130)	1.56 (210)
	1.60	90	4.9	39.1	SU	1.60 (140)	2.36 (210)
	1.70	90	7.4	41.9	SU	2.20 (130)	3.24 (210)

Close to the drainage face, the seepage vector is at $180 \leqslant \lambda \leqslant 270$ and the valid failure plane is $x-x$ (see Fig. 4). Lambda (λ) is approximated from maximum seepage vector simulated by the two-dimensional seepage model (SEEP/W).
[a] PO = Tension or ''pop-out'' failure.
[b] SU = Failure included seepage particle mobilization and undercutting.

When cohesion was considered, sand at ρ_b = 1.30 Mg m^{-3} was unstable close to the inlet and at the drainage face. The instability close to the inlet caused the tension or ''pop-out'' failures observed during the experiments. The bank collapsed before seepage erosion undercutting could initiate. At ρ_b = 1.45 Mg m^{-3}, there were some values of λ which could also result in tension or ''pop-out'' failure. However,

during the experiment, the gradient may have been lower than the limiting value of λ for instability, causing the bank to hold until the initiation of seepage erosion.

The loamy sand showed consistent stability at both locations except for ρ_b = 1.50 Mg m^{-3} close to the inlet which could be unstable if $\lambda \leqslant 130$ degrees. Simulations from the two-dimensional model predicted a λ of approximately
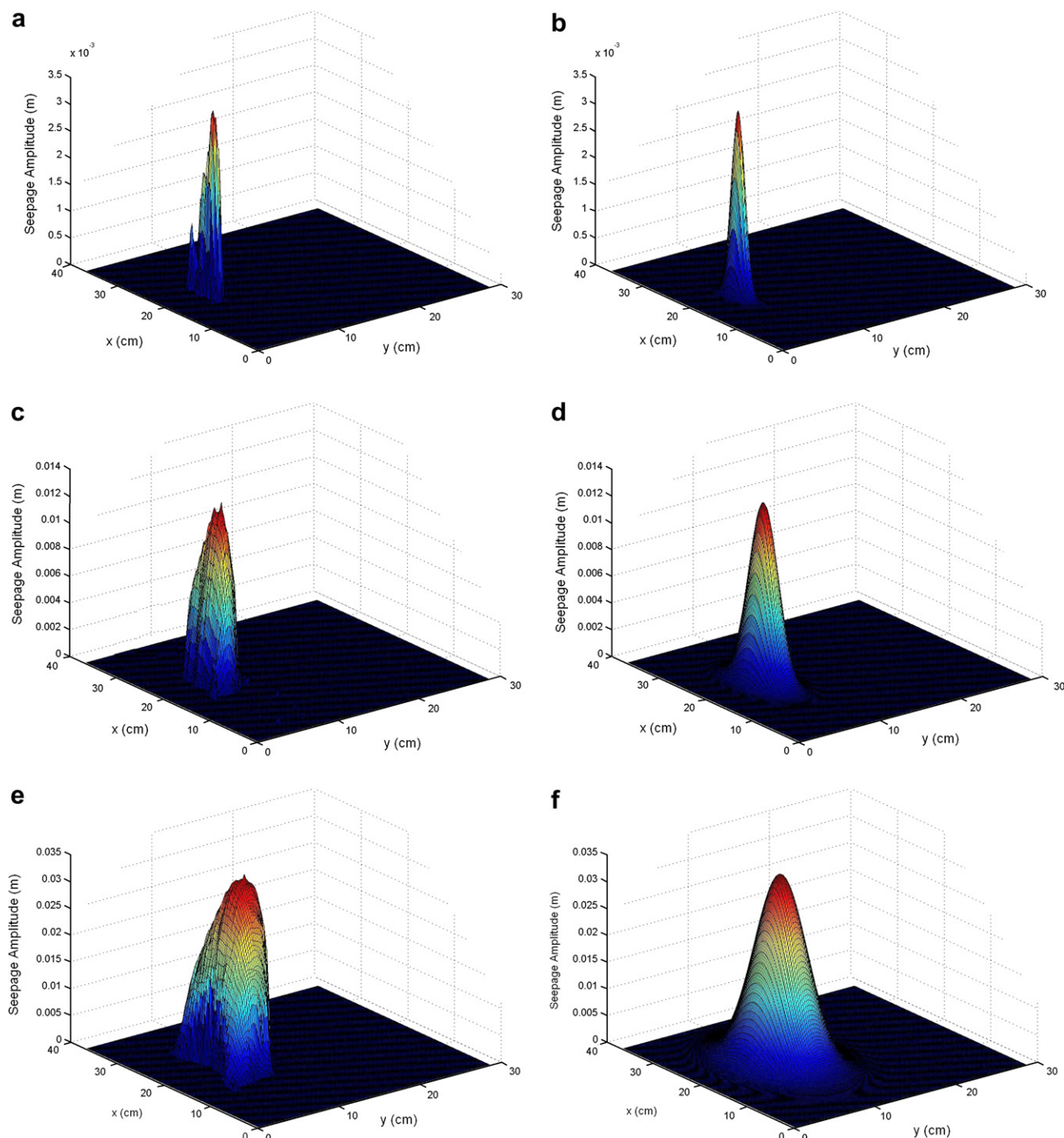

Figure 6 Typical time sequence of seepage erosion headcut formation. Note that the x—y plane is the bank face. Example shown is for the case of a 90° sand bank, 35 cm water head with ρ_b = 1.60 Mg m^{-3}. (a) t = 108 s after flow arrival, (b) Gaussian fit for t = 108 s (R^2 = 0.80), (c) t = 125 s after flow arrival, (d) Gaussian fit for t = 125 s (R^2 = 0.77), (e) t = 149 s after flow arrival, and (f) Gaussian fit for t = 149 s (R^2 = 0.78).

$130°$ for the maximum seepage vector close to the inlet. Banks with ρ_b equal to 1.60 Mg m^{-3} and 1.70 Mg m^{-3} on the other hand were stable at both locations causing the bank to hold until seepage erosion undercutting initiated.

Unimodal versus multimodal seepage erosion headcuts

For cases in which the seepage process was by seepage erosion and undercutting, it was observed during the experiments that seepage erosion could initiate as a unimodal headcut in which erosion was concentrated at one location on the bank face or as a multimodal headcut in which erosion initiated at different locations on the bank face. Results were consistent among duplicate experiments for each set of experimental conditions. A typical time sequence demonstrating the changes in the seepage headcut as seepage erosion progressed is shown in Fig. 6 for the case of a unimodal headcut. Also shown is the Gaussian fit for these specific headcuts. The strength of the fit, quantified through calculation of the coefficient of determination, or R^2, was greater in cases where the seepage erosion headcuts initiated at one location on the bank face.
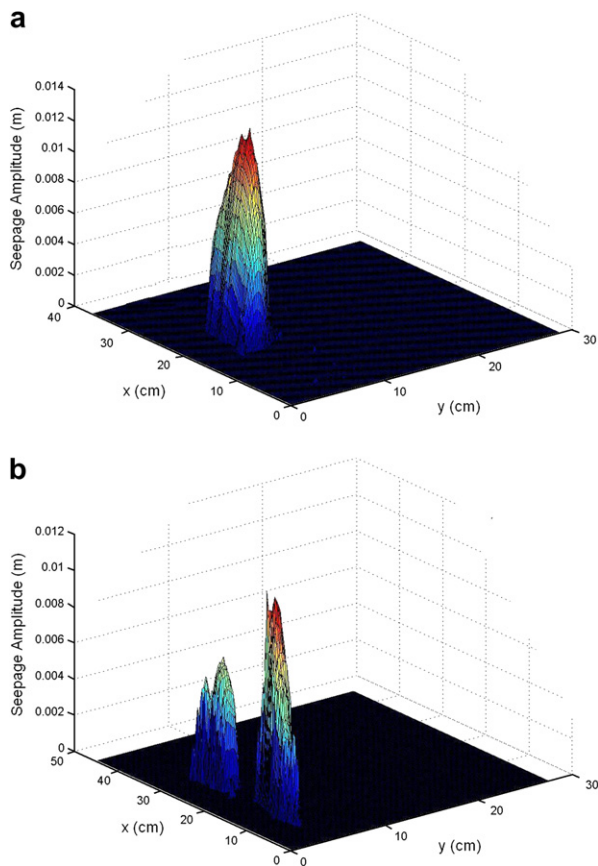
It was hypothesized that multimodal headcuts would form in experiments with lower α', lower ρ_b, and lower inflow H. However, for these experimental conditions, the mode of initial seepage erosion undercutting was controlled by α'. A $90°$ bank, regardless of the H, ρ_b, and soil type, started with unimodal erosion while banks with α' of less than $90°$ (i.e., $75°$ and $60°$) started with multimodal erosion. The $90°$ banks manifested in initial unimodal headcuts horizontally centered along the bank face while the $75°$ and $60°$ banks started with multimodal headcuts which initiated at random locations within the seepage layer (Fig. 7), with the locations potentially corresponding to micro-scale preferential flow features created during packing.

The multimodal headcuts generally converged into unimodal headcuts, with this convergence time hypothesized to depend on soil type, ρ_b, α', and inflow H. For α' less than $90°$, convergence was identified from the scanned images and was verified using the regression coefficient from the fit of the Gaussian function to the three-dimensional undercut shape. An R^2 of at least 0.70 was used as an identifier for convergence. The time for the multimodal headcuts to converge to a concentrated unimodal erosion headcut was prominently controlled by the inflow H. The higher the H the less time it took for convergence to occur for both soil types at different ρ_b (Fig. 8). Contrary to initial hypotheses,

Figure 7 Example of: (a) unimodal and (b) multimodal seepage erosion headcuts. Note that the $x-y$ plane is the bank face. The unimodal figure is for the case of loamy sand with $90°$ bank, 35 cm head, and 1.60 Mg m^{-3} bulk density. The bimodal figure is for the loamy sand with $75°$ bank, 15 cm head, and 1.70 Mg m^{-3} bulk density.
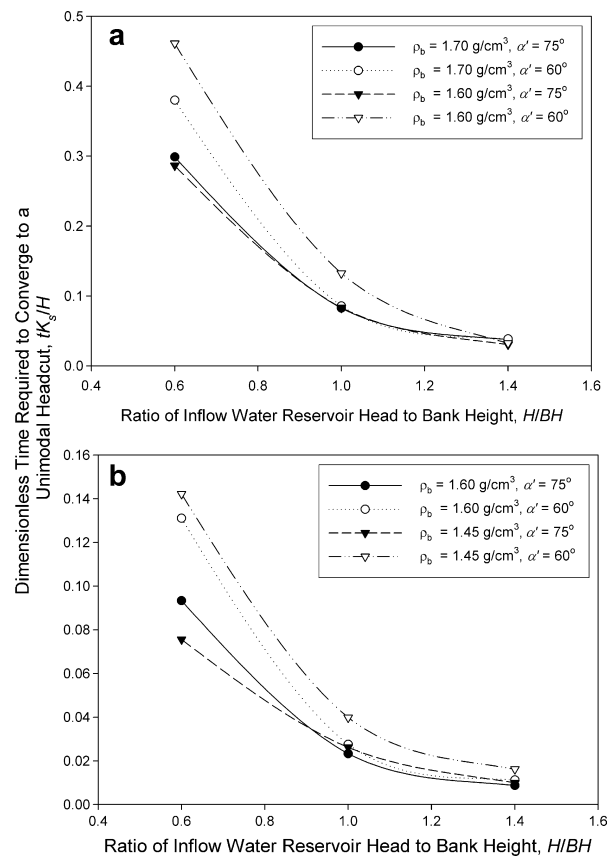

Figure 8 Time required for multimodal seepage particle mobilization headcuts for: (a) sand and (b) loamy sand soils to reach unimodal headcut, non-dimensionalized by the saturated hydraulic conductivity, K_s, and the water inflow reservoir head, H.

convergence time was more dependent on α' than ρ_b for the range of ρ_b investigated in this research. Convergence times as a function of H were approximately equivalent for the same soil with different ρ_b but the same α'. Once converged, the resulting unimodal headcut possessed greater lateral spreads (i.e., larger σ_x), sometimes extending the entire width of the bank face.

Trends in seepage erosion undercut shapes

For a given headcut amplitude (A), the width of the undercut (i.e., σ_x) was approximately an order of magnitude greater than the height (i.e., σ_y) of the undercut (Fig. 9). At a given A, slightly larger σ_x and σ_y were observed for the loamy sand as compared to the sand soil due to the cohesive strength of the materials. Regression curves through the $\sigma_y - A$ data demonstrated similar power-curve relationships for the sand and loamy sand soils. Statistical tests based on non-linear analysis of covariance (Hinds and Milliken, 1987) suggested no significant difference between the $A - \sigma_y$ relationships for the two soil types (F-value of 2.00, P-value of 0.16 at a significance level of 0.05).

The $\sigma_y - A$ relationships consisted of greater scatter but still demonstrated a fairly uniform pattern between the two soil types. In fact, the sand soils typically followed a strong linear relationship before experiencing data scatter for $A > 4$ cm. The outliers in $\sigma_x - A$ (Fig. 9b) corresponded to measurements of large amplitude undercutting just prior to failure during those experiments with greater stability (i.e., higher ρ_b and lower α'). The scatter from a linear trend line started at smaller A for the loamy sand soil (i.e., $A > 1$ cm). Differences in the $A - \sigma_x$ relationships for the sand and loamy sand soils were less apparent at lower A. Statistical tests using analysis of covariance on the $A - \sigma_x$ relationships suggested significant differences between the two soil types (P-value less than 0.001 at significance level of 0.05); however, from a stability perspective, the differences in the predicted widths (i.e., on the order of cm) would not be significant for A less than 10 cm.

These common relationships, especially in the $\sigma_y - A$, were most likely functions of the similar c' (i.e., less than 7.5 kPa) and φ' (i.e., between 25° and 40°) between the two soils. No apparent dependency of the $\sigma_y - A$ and $\sigma_x - A$ relationships on ρ_b was observed when analyzing the data. These results suggest that it may be possible to use such generalized relationships as a first approximation for inclusion of seepage particle mobilization and undercutting in stability models.

Summary and conclusions

Seepage mechanisms of hillslope, gully, and streambank instability include: (1) tension or ''pop-out'' failure when the seepage forces are greater than the soil resistance as well as reduced shear strength from increased soil pore-water pressure, and (2) particle mobilization (i.e., entrainment in seepage flow) and bank undercutting when the seepage force gradient was less than the resisting force of the soil block with eventual bank collapse due to the combined forces from seepage undercutting, seepage forces, and the buildup of pore-water pressure. The first type of
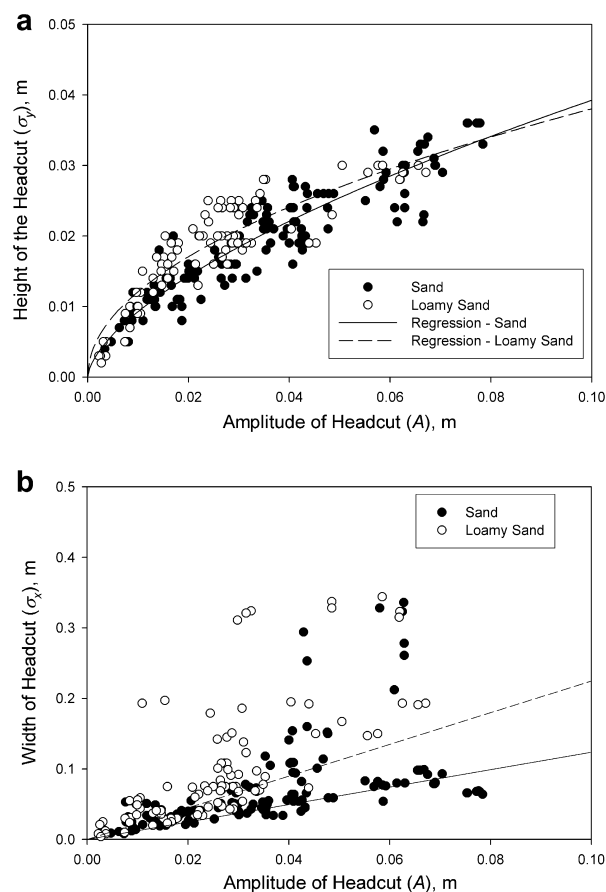
Figure 9   Observed relationship between the amplitude (A) of the headcut and the (a) height as quantified by the spread (i.e., σ_y), and (b) width of the headcut (σ_x) for the sand and loamy sand soils. Note that the regression lines shown for σ_x versus A are for A less than 4 cm.

failures (tension or ''pop-out'') have been analyzed from a geotechnical point of view where the driving static forces exceed the resisting static forces resulting in a block failure with tension crack formation, with the necessity of considering cohesion effects due to packing. The later mechanism occurred when the bank's shear strength was great enough to resist initial tension or ''pop-out'' failure of the bank. Seepage velocities became greater than critical velocities necessary for particle mobilization leading to particle entrainment in the seepage flow, undercutting and bank collapse. The undercutting acted in conjunction with reduced shear strength due to increased soil pore-water pressure and the seepage force due to the hydraulic gradient. Within a specific soil type, the occurrence of these mechanisms was largely controlled by the soil's bulk density, which directly influenced the hydraulic conductivity, effective cohesion, internal angle of friction, and critical shear stress.

For banks experiencing seepage particle entrainment and undercutting, the slope of the bank predominately influenced the undercutting formation. For these experimental conditions, unimodal headcuts were observed throughout the experiment for banks with 90° slopes. On banks with smaller slopes, the headcuts generally initiated as multi-

modal, eventually converting to a unimodal headcut sometime before bank failure and controlled largely by the hydraulic gradient and the bulk density.

Relationships were developed between the amplitude, width, and height of the headcut for both the sand and loamy sand soils investigated in this research. A power law relationship was observed between amplitude and height with the relationship fairly equivalent for both soils. Differences in soil type were more prevalent in the relationships between amplitude and width. While the differences (i.e., on the order of cm) between soil types were statistically significant, it is hypothesized that they would not be significant from a stability perspective. These generalized relationships could be used to predict the width and height of the undercut based on a priori knowledge of the amplitude. The fact is important for the eventual incorporation of this seepage mechanism into stability models.

Acknowledgments

References

Abam, T.K.S., 1993. Factors affecting distribution of instability of river banks in the Niger delta. Engineering Geology 35, 123—133.

ASCE Task Committee on Hydraulics, Bank Mechanics, and Modeling of River Width Adjustment. 1998. River width adjustment. I: Processes and mechanisms. Journal of Hydraulic Engineering-ASCE 124(9), 881-902.

Bradford, J.M., Piest, R.F., 1977. Gully wall stability in loess derived alluvium. Soil Science Society of America Journal 41 (1), 115—122.

Budhu, M., Gobin, R., 1996. Slope stability from ground-water seepage. Journal of Hydraulic Engineering-ASCE 122 (7), 415—417.

Chu-Agor, M., Wilson, G.V., Fox, G.A., in press. Numerical modeling of bank instability by seepage erosion. Journal of Hydrologic Engineering.

Crosta, G., di Prisco, C., 1999. On slope instability induced by seepage erosion. Canadian Journal of Geotechnical Engineering 36, 1056—1073.

Darby, S.E., Thorne, C.R., 1996. Numerical simulation of widening and bed deformation of straight sand-bed rivers. I. Model development. Journal of Hydraulic Engineering 122, 184—193.

Faulkner, H., 2006. Piping hazard on collapsible and dispersive soils in Europe. In: Boardman, J., Poesen, J. (Eds.), Soil Erosion in Europe. John Wiley and Sons, Inc., West Sussex, England.

Fox, G.A., Wilson, G.V., Periketi, R.K., Cullum, B.F., 2006. A sediment transport model for seepage erosion of streambanks. Journal of Hydrologic Engineering — ASCE 11 (6), 603—611.

Fox, G.A., Wilson, G.V., Simon, A., Langendoen, E., Akay, O., Fuchs, J.W., 2007a. Measuring streambank erosion due to ground water seepage: correlation to bank pore water pressure, precipitation, and stream stage. Earth Surface Processes and Landforms 32 (10), 1558—1573.

Fox, G.A., Chu-Agor, M., Wilson, G.V., 2007b. Erosion of non-cohesive sediment by groundwater seepage flow: experiments and numerical modeling. Soil Science Society of America Journal 71 (6), 1822—1830.

Fredlund, D.G., Rahardjo, H., 1993. Soil Mechanics for Unsaturated Soils. John Wiley and Sons, New York.

Hinds, M.A., Milliken, G.A., 1987. Statistical methods for using non-linear models to compare silage treatments. Biometrical Journal 29 (7), 825—834.

Hooke, J.M., 1979. An analysis of the processes of river bank erosion. Journal of Hydrology 42, 39—62.

Howard, A.D., McLane III, C.F., 1988. Erosion of cohesionless sediment by ground water seepage. Water Resources Research 24 (10), 1659—1674.

Lindow, N., 2007. Channel evolution of a restored low gradient, sand bed stream. Ph.D. Dissertation, North Carolina State University, Raleigh, NC.

Lobkovsky, A.E., Jensen, B., Kudrolli, A., Rothman, D.H., 2004. Threshold phenomena in erosion driven by subsurface flow. Journal of Geophysical Research-Earth Surface 109(F4), Art. No. F04010.

Lourenco, S.D.N., Sassa, K., Fukuoka, H., 2006. Failure process and hydrologic response of a two layer physical model: implications for rainfall-induced landslides. Geomorphology 73, 115—130.

McWhorter, D.B., Sunada, D.K., 1977. Ground-Water Hydrology and Hydraulics. Water Resources Publications, Highland Park, Colorado.

Rinaldi, M., Casagli, N., 1999. Stability of streambanks formed in partially saturated soils and effects of negative pore water pressures: the Siene River (Italy). Geomorphology 26, 253—277.

Rinaldi, M., Casagli, N., Dapporto, S., Gargini, A., 2003. Monitoring and modeling of pore water pressure changes and riverbank stability during flow events. Earth Surface Processes and Landforms 29, 237—254.

Simon, A., Curini, A., Darby, S.E., Langendoen, E.J., 1999. Streambank mechanics and the role of bank and near-bank processes in incised channels. In: Darby, SE., Simon, A. (Eds.), Incised River Channels. John Wiley and Sons, Chichester, UK, pp. 193—217.

Sultan, N., Cochonat, P., Canals, M., Cattaneo, A., Dennielou, B., Haflidason, H., Laberg, J.S., Long, D., Mienert, J., Trincardi, F., Urgeles, R., Vorren, T.O., Wilson, C., 2004. Triggering mechanisms of slope instability processes and sediment failures on continental margins: a geotechnical approach. Marine Geology 213, 291—321.

van Genuchten, M.Th., Leij, F.J., Yates, S.R., 1991. The RETC Code for Quantifying the Hydraulic Functions of Unsaturated Soils. United States Environmental Protection Agency (USEPA) 000/ 091/000, USEPA, Ada, OK.

Weisstein, E.W., 1999. Gaussian function. In: CRC Concise Encyclopedia of Mathematics. CRC Press, New York, pp. 716—717.

Whitlow, R., 1983. Basic Soil Mechanics. Construction Press, New York.

Wilson, G.V., Periketi, R., Fox, G.A., Dabney, S., Shields, D., Cullum, R.F., 2007. Seepage erosion properties contributing to streambank failure. Earth Surface Processes and Landforms 32 (3), 447—459.